Research Square

Preprints are preliminary reports that have not undergone peer review.
They should not be considered conclusive, used to inform clinical practice,
or referenced by the media as validated information.

Integrated Simulation-Based Trajectory and Actuator Design for a 6-DoF Manipulator via Workspace-Aware Pareto Optimization and PMSM–FOC–CTC

Ojonugwa Adukwu

ojonugwa.adukwu@alumni.usp.br

Universidade de São Paulo

Fabio de Oliveira Fialho

Universidade de São Paulo

Fuad Kassab Junior

Universidade de São Paulo

Beatriz Barbuy

Universidade de São Paulo

Research Article

Keywords: Robotic manipulator; workspace-aware optimization; Pareto trajectory selection; actuator design; PMSM–FOC; computed-torque control

Posted Date: November 10th, 2026

DOI: https://doi.org/10.21203/rs.3.rs-11653673/v1

License: This work is licensed under a Creative Commons Attribution 4.0 International License.
Read Full License

Additional Declarations: No competing interests reported.

Integrated Simulation-Based Trajectory and Actuator Design for a 6-DoF Manipulator via Workspace-Aware Pareto Optimization and PMSM–FOC–CTC

Ojonugwa Adukwu [1,*]
Fábio de Oliveira Fialho [1]
Fuad Kassab Junior [1]
Beatriz Barbuy [2]

[1] Polytechnic School, Department of Electrical Engineering, University of São Paulo, São Paulo, Brazil
[2] Institute of Astronomy, Geophysics and Atmospheric Sciences, Department of Astronomy, University of São Paulo, São Paulo, Brazil

ojonugwa.adukwu@alumni.usp.br
fabio.fialho@usp.br
fuad@lac.usp.br
b.barbuy@iag.usp.br

Abstract Workspace characterization, trajectory selection, actuator sizing, and closed-loop control are interdependent but are frequently assessed separately. This paper develops an integrated simulation-based task-to-actuator design framework for a six-degree-of-freedom manipulator carrying an 18-kg payload. A study of 50,000 robot configurations identifies overlapping but independently classified high-quality (5,001) and screened-Pareto (1,094) workspace subsets. Independently generated inverse-kinematics seeds produce 24 candidate trajectories, of which 11 satisfy joint-space continuity requirements and eight meet dense full-pose tolerances. Dynamic Pareto evaluation of the eight feasible trajectories retains two nondominated representatives, C3 and C24. They reflect different peak-torque, RMS-torque, and mechanical-work demands. These alternatives inform a manufacturer-constrained motor–gearbox search and multi-rate PMSM–FOC–CTC simulation. Four six-second letter-E scenarios provide two controlled comparisons. Under common H1 actuator architecture and G2 controller gains, reference corner rounding reduces Cartesian tracking RMSE from 44.5767 to 3.4071 mm. Under common A218 architecture and G2 controller gains, the C24-based scenario achieves an RMSE of 1.7411 mm compared with 1.9781 mm for the C3-based scenario. The results distinguish local workspace quality from complete-trajectory feasibility. They demonstrate the importance of retaining alternative trajectories through actuator selection and closed-loop validation. Cross-architecture comparisons remain descriptive rather than isolated trajectory-effect tests. Future work will address repeated-duty thermal assessment and experimental validation.

Keywords: Robotic manipulator; workspace-aware optimization; Pareto trajectory selection; actuator design; PMSM–FOC; computed-torque control.

1 Introduction

Industrial robot manipulators must meet several requirements at the same time. These include workspace reach, payload capacity, motion accuracy, and actuator operating limits. However, satisfying one requirement does not guarantee that the others will be satisfied. For example, a robot may reach a desired position but have poor motion capability in certain directions. Similarly, a continuous joint-space trajectory may require more torque than the actuators can provide. Even when a motor–gearbox combination satisfies mechanical requirements, it may still violate electrical limits or experience difficulties during closed-loop control [1–3].

For these reasons, trajectory planning involves more than finding a geometric path between positions. The designer must also consider how long the motion takes, the required joint torques, the smoothness of the motion, and measures related to energy demand [4–7]. Previous studies have investigated actuator sizing based on trajectory requirements and the combined design of motion, motors, and controllers [3, 8–10]. These studies motivate an integrated approach in which the effects of trajectory selection are examined from the initial Cartesian task to the final electromechanical simulation.

An important part of this approach is understanding the difference between geometric reachability and usable workspace. Geometric reachability describes where the robot can position its tool within its joint limits. However, reaching a position does not necessarily mean that the robot can operate there effectively. For example, increasing the payload changes the gravitational forces and torques acting on the joints. It also changes the remaining torque capacity available for motion. However, it does not change the geometric workspace when the robot geometry and joint limits remain fixed.

The translational Jacobian provides additional information about the robot's motion capability at a particular configuration. It can be used to evaluate local dexterity, proximity to singularities, and how joint-position errors affect the tool-center-point (TCP) position [11–13]. Therefore, workspace evaluation should

consider geometric reach, kinematic performance, and payload-related loading together. The robot configurations used to perform a task also affect the joint torques required during the motion [14, 15].

A Cartesian task can often be performed using several different continuous joint-space trajectories. Although these trajectories produce the required Cartesian motion, they may differ in total joint travel, torque demand, and mechanical work. For example, a trajectory that requires the lowest peak joint-torque demand may not require the lowest root-mean-square (RMS) torque or mechanical work. Therefore, selecting only one inverse-kinematic solution or combining several objectives into a weighted score too early may hide useful alternatives [7, 16, 17].

Pareto analysis provides a way to retain these alternatives without assigning preference weights to the objectives. A trajectory is considered nondominated when no other evaluated trajectory performs at least as well in every objective and strictly better in at least one objective. The resulting nondominated trajectories represent different compromises among the design objectives [18, 19].

This paper develops an integrated task-to-actuator design framework for a six-degree-of-freedom (six-DoF) robot manipulator. The framework begins by defining the robot dynamic model, design variables, constraints, and evaluation measures. It then characterizes the robot's reachable workspace and local motion capability before generating alternative joint-space trajectories.

The generated trajectories are screened for continuity and evaluated using four robot-side dynamic objectives. Pareto analysis is used to retain trajectories with different torque and mechanical-work characteristics. Workspace-quality measures provide additional information for interpreting these alternatives, but they are not included directly in the four-objective dynamic Pareto calculation.

The retained trajectories are then used to select suitable motor–gearbox combinations from manufacturer specifications. The resulting actuator architectures are evaluated using an integrated robot–gearbox–permanent-magnet synchronous motor (PMSM) model. The model includes field-oriented control (FOC) for motor current regulation and computed-torque control (CTC) for robot motion tracking. All validation results presented in this study are obtained through MATLAB and Simulink simulations [20, 21].

The main contribution of this work is a traceable design framework that connects analysis stages often considered separately.

In particular, the workspace analysis produces two different but overlapping classifications: a high-quality workspace subset and a screened workspace-Pareto subset. These classifications are obtained in parallel rather than through successive filtering steps. The initial trajectory candidates are generated independently of these classifications. Their starting configurations are subsequently compared with the workspace subsets, and the complete trajectories are screened for joint-space continuity and dense Cartesian full-pose accuracy.

This approach distinguishes the quality of an individual robot configuration from the feasibility and performance of a complete trajectory. The framework also preserves different inverse-kinematic solutions and evaluates peak aggregate torque, RMS aggregate torque, and mechanical work without assigning arbitrary objective weights. The workspace characteristics of the candidate trajectories are then interpreted alongside their dynamic performance. Selected trajectories are carried forward into actuator architecture selection and multi-rate closed-loop simulation.

In addition, four letter-E motion scenarios are compared to examine the effects of trajectory corner treatment and actuator architecture on Cartesian tracking. The comparisons distinguish changes caused by the trajectory within a common actuator and controller configuration from differences involving distinct actuator architectures. Thus, not every difference in tracking performance is attributed to trajectory optimization alone.

The results provide a foundation for future human–machine interface (HMI) development and the development of a collaborative robot (CoBoT). The framework is also intended for extension to the robotic subsystem of the Multi-Object Spectrograph for Astrophysics, Intergalactic-medium studies and Cosmology (MOSAIC) positioner [22] , supporting further development of the work reported in [23]. Figure 1 summarizes the proposed methodology. The letter-E task is introduced in Section 6 as a demonstration of the general methods.

The remainder of this paper is organized as follows. Section 2 defines the manipulator model and design problem. Section 3 presents workspace characterization and trajectory generation. Section 4 develops workspace-aware Pareto trajectory evaluation. Section 5 describes actuator selection and the PMSM–FOC–CTC model. Section 6 presents and discusses the workspace, trajectory, actuator-selection, and closed-loop simulation results, including the four-scenario Cartesian tracking comparison. Section 7 discusses limitations and reproducibility, and Section 8 concludes the paper.

2 System Model

This section introduces the physical and mathematical models used in the proposed task-to-actuator design framework. The robot dynamics and friction model are first defined to determine the torques required at the joints. The manipulator geometry and payload are then specified to establish the robot's motion and loading conditions. Finally, the design variables, operating constraints, and performance measures are introduced. These provide a common basis for workspace analysis, trajectory optimization, actuator selection, and closed-loop validation in the following sections.

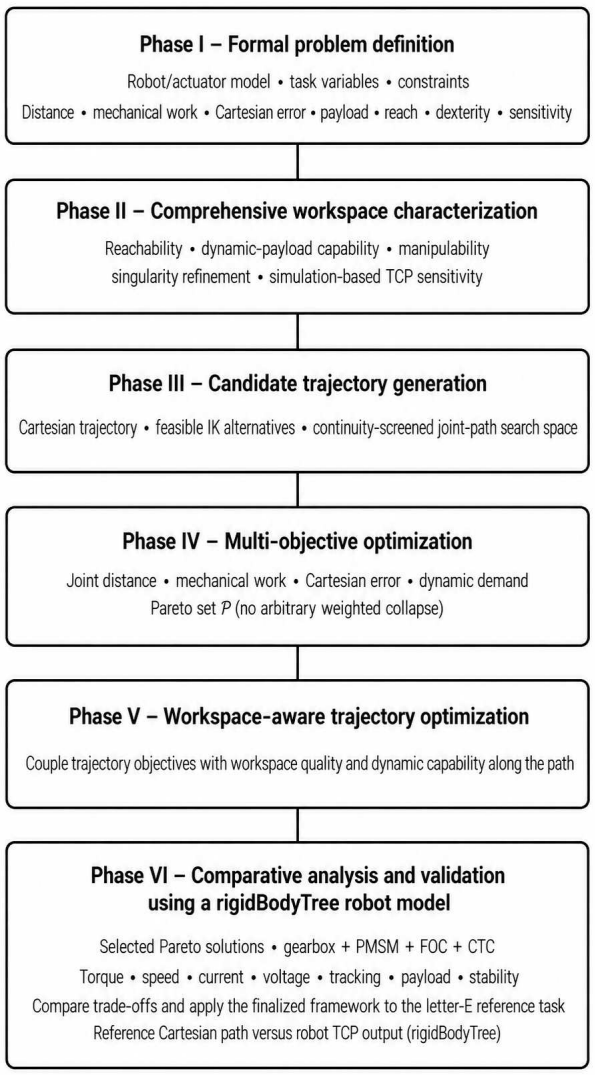


Figure 1: Governing research framework. Workspace characterization and trajectory analysis feed workspace-aware Pareto evaluation, actuator architecture selection, and electromechanical simulation validation.

2.1 Rigid-body dynamics and friction

The motion of the manipulator is described by the standard rigid-body dynamic equation [24]

$$M(q)\ddot{q} + c(q,\dot{q}) + g_q(q) + \tau_f(\dot{q}) = \tau_d, \tag{1}$$

where q, $\dot{q}$, and $\ddot{q}$ are the vectors of joint positions, velocities, and accelerations, respectively.

The matrix $M(q)$ represents the robot's inertia, which depends on its joint configuration. The vector $c(q,\dot{q})$ contains the Coriolis and centrifugal torques associated with joint motion, while $g_q(q)$ represents the torques caused by gravity. The vector $\tau_f(\dot{q})$ describes joint friction, and τ_d is the torque delivered to the robot joints after the transmission. Equation (1) shows how the required joint torque depends on robot acceleration, joint motion, gravity, and friction. It is therefore used to calculate the torque requirements of candidate trajectories and to develop the computed-torque controller.

At this stage, $M(q)$ includes the rigid-body inertia of the manipulator and its attached payload. The additional inertia introduced by the motors through the gearboxes is included later in the electromechanical model of Section 5.

For numerical simulation, joint friction is represented using a smooth Coulomb–viscous model [25, 26]

$$\tau_{f,j} = T_{c,j}\tanh\left(\frac{\dot{q}_j}{v_{s,j}}\right) + B_{v,j}\dot{q}_j, \tag{2}$$

where $T_{c,j}$ represents the Coulomb-friction magnitude at joint j, $B_{v,j}$ is the viscous-friction coefficient, and $v_{s,j}$ determines how quickly the friction model changes around zero velocity. The model contains two friction components. The first represents Coulomb friction, which opposes joint motion. The second represents viscous friction, which increases with joint velocity. The hyperbolic-tangent function provides a smooth approximation of Coulomb friction near zero velocity. Unlike the sign function, it does not change abruptly when the joint velocity crosses zero. This smooth transition reduces numerical switching effects during simulation while preserving the main behavior of Coulomb friction at velocities away from zero. It is especially useful when a trajectory causes a joint to reverse its direction of motion repeatedly.

The adopted Coulomb-friction parameters are

$$T_c = [2,\ 4,\ 2,\ 0.8,\ 0.5,\ 0.3]^T\ \mathrm{N\,m}, \tag{3}$$

and the viscous-friction parameters are

$$B_v = [0.20,\ 0.40,\ 0.20,\ 0.08,\ 0.05,\ 0.03]^T\ \mathrm{N\,m\,s/rad}, \tag{4}$$

with $v_s = 0.02$ rad/s.

These values are engineering assumptions adopted for simulation. They are not friction parameters obtained from experimental identification or manufacturer measurements. Using the same friction model throughout the study provides consistent conditions for comparing the candidate trajectories and actuator designs.

2.2 Manipulator geometry and payload

The manipulator has six revolute joints. Its joint-position vector is defined as $\mathbf{q} = [q_1,\ldots,q_6]^T$. The robot geometry is described using the Denavit–Hartenberg (DH) parameters, which define the relative positions and orientations of successive joint frames.

The adopted DH parameters are

$$\mathbf{a} = \begin{bmatrix}0, -0.5068, -0.3616, 0, 0, 0\end{bmatrix}^T\ \mathrm{m}, \tag{5}$$

$$\mathbf{d} = \begin{bmatrix}0.2186 & 0 & 0 & 0.1824 & 0.1361 & 0.1413\end{bmatrix}^T\ \mathrm{m}, \tag{6}$$

$$\boldsymbol{\alpha} = [\pi/2, 0, 0, \pi/2, -\pi/2, 0]^T. \tag{7}$$

The vector $\mathbf{a}$ contains the link-length parameters, $\mathbf{d}$ contains the link-offset parameters, and $\boldsymbol{\alpha}$ contains the link-twist angles. The gravitational acceleration

vector is $\mathbf{g} = [0, 0, -9.81]^T$ m/s^2. The tool-center point (TCP), which is the reference point used to describe the task, coincides with the origin of frame {6}.

An 18-kg payload is attached to the manipulator. Its center of mass is located at $[0, 0, 0.163]^T$ m relative to frame {6}. The robot geometry and payload remain unchanged throughout the workspace and trajectory analyses. Therefore, the optimization does not modify the robot's link dimensions or joint arrangement. Instead, it identifies feasible joint-space trajectories and suitable motor–gearbox architectures for the specified manipulator.

2.3 Decision variables, constraints, and performance measures

The design framework uses several quantities to evaluate robot performance. These quantities are grouped according to their roles in workspace analysis, trajectory evaluation, and actuator selection. This distinction is important because a quantity used to describe workspace quality is not necessarily an optimization objective or an actuator operating constraint. Workspace analysis first examines geometric reach, local motion capability, and payload-dependent joint loading.

Geometric reach describes the TCP positions that the robot can attain within its joint limits. However, reaching a position does not necessarily mean that the robot can perform a task there under the available actuator limits. For this reason, payload-related joint torques and available actuator capacity are considered separately when evaluating dynamic workspace capability.

Increasing the payload changes joint loading and the remaining torque capacity available for motion. However, it does not change the geometric workspace when the manipulator geometry and joint limits remain fixed. The translational Jacobian is used to evaluate local manipulability and proximity to singular configurations. It is also used to estimate how small joint-position errors affect the TCP position. This quantity is called joint-position-error-to-TCP sensitivity in the present study. Although it was previously described as "repeatability" during model development, it does not represent experimentally measured robot repeatability. Instead, it predicts the TCP-position variation associated with a prescribed joint-position uncertainty.

Trajectory performance is evaluated using joint travel, torque requirements, mechanical work, and Cartesian tracking accuracy. For a discrete joint-space path, joint travel is calculated from the accumulated joint-position increments. The mechanical power at joint j is

$$P_j(t) = \tau_j(t)\dot{q}_j(t).$$

The trajectory evaluation uses positive mechanical work and absolute mechanical work as two separate measures. Positive mechanical work accumulates the work performed when joint mechanical power is positive. Absolute mechanical work accumulates the magnitudes of both positive and negative mechanical power. These quantities describe mechanical energy transfer at the robot joints. They do not represent the electrical energy consumed by the motors and inverters. Cartesian tracking accuracy is evaluated using the TCP-position error

$$e_p(t) = \|\mathbf{p}_d(t) - \mathbf{p}(t)\|_2 ,$$

where $\mathbf{p}_d(t)$ is the desired TCP position and $\mathbf{p}(t)$ is the actual TCP position. This error measures the distance between the desired and actual TCP positions at each instant.

Finally, actuator feasibility is evaluated using manufacturer-specified torque, speed, and electrical operating limits. Peak torque and current ratings describe the maximum permitted short-duration operating demands. Continuous ratings describe the actuator's ability to sustain loading during longer operating periods. Therefore, satisfying peak operating limits during a short simulation does not, by itself, demonstrate that the actuator can operate repeatedly without excessive heating.

Together, these definitions provide a consistent basis for workspace characterization, trajectory screening, multi-objective optimization, actuator selection, and closed-loop validation in the following sections.

3 Workspace and Trajectories

This section explains two analyses used before trajectory optimization. The first examines where the robot can reach and how well it can move at different joint configurations. It considers geometric reach, translational dexterity, proximity to singularities, payload loading, and the effect of joint-position errors on the tool-center-point (TCP) position. The second analysis finds different joint-space paths that can perform a prescribed Cartesian task. These analyses are carried out separately and are brought together in Section 4. A good individual robot configuration does not necessarily lead to a feasible complete trajectory.

3.1 Reachable workspace

For a joint configuration q, forward kinematics gives the TCP position:

$$p = f_{\mathrm{FK}}(q). \tag{8}$$

The geometric workspace is estimated by sampling 50,000 joint configurations within the specified joint limits. A fixed random seed of 18 is used so that the numerical sampling can be repeated [27]. The TCP positions obtained from these configurations are used to estimate the workspace boundaries, the distribution of distances from the robot base, and the convex-hull volume.

The convex hull is an outer envelope around the sampled TCP positions, not an exact description of the reachable workspace. A point inside this envelope is not necessarily reachable or collision-free. Even if

it is reachable, the robot may have poor motion capability or insufficient dynamic capability at that point [28]. The 50,000 sampled configurations form a common reference population for the subsequent analyses of dexterity, payload sensitivity, and workspace quality. The numerical results are presented in Section 6.

3.2 Dexterity and singularity analysis

The translational Jacobian $J_v(q)$ relates joint velocities to the TCP's linear velocity:

$$\dot{p} = J_v(q)\dot{q}. \tag{9}$$

The Jacobian is used to examine how easily the robot can produce TCP motion in different directions. Let its singular values be ordered as

$$\sigma_1 \geq \sigma_2 \geq \sigma_3. \tag{10}$$

The smallest singular value is

$$\sigma_{\min} = \sigma_3. \tag{11}$$

It describes the weakest local direction for generating translational velocity. As $\sigma_{\min}$ approaches zero, the configuration approaches a translational kinematic singularity.

Translational manipulability is defined as [12]

$$\mu_v = \sqrt{\det\left(J_v J_v^T\right)} = \sigma_1\sigma_2\sigma_3, \tag{12}$$

and the translational condition number is

$$\kappa_v = \frac{\sigma_{\max}}{\sigma_{\min}}. \tag{13}$$

Manipulability describes the overall local ability to generate TCP translation, while the condition number indicates how evenly this ability is distributed across directions. A small $\sigma_{\min}$, low μ_v, or large κ_v indicates an unfavorable aspect of local translational motion capability. These quantities describe translation only; they do not, by themselves, establish dexterity for the complete six-dimensional TCP pose.

Random sampling provides a broad picture of workspace quality but may miss small regions close to singularities. To investigate such regions more closely, targeted numerical refinement starts from the 20 sampled configurations with the smallest $\sigma_{\min}$ values. The resulting statistics and refined singularity assessment are reported in Section 6.

3.3 Payload and joint-position-error sensitivity

Payload loading is evaluated separately from geometric reach. For each sampled configuration, the joint torques caused by the payload are calculated and compared with the available actuator torque capability. Payload sensitivity describes how much the required joint torque changes when payload mass changes [29, 30]. This analysis identifies configurations that place greater demands on the actuators. Payload loading can reduce the torque reserve available for motion and therefore affect the dynamically usable workspace. However, it does not change the geometric workspace when the robot geometry and joint limits remain fixed.

The effect of joint-position errors on TCP position is examined separately. For a small joint-position error δq, the first-order approximation is [31]

$$\delta p \approx J_v(q)\,\delta q. \tag{14}$$

The analysis assumes an independent joint-position uncertainty of 1 arcmin for each joint at every sampled configuration. The resulting measure estimates how these joint-position errors may affect TCP position. It is a model-based sensitivity measure, not an experimentally measured repeatability value. The payload-loading and TCP-sensitivity results are reported in Section 6.

3.4 Multi-metric dexterous-workspace screening

A reachable configuration is not necessarily a good configuration for performing a task. Each sampled configuration is therefore assessed using four measures: translational manipulability, minimum singular value, payload-sensitivity norm, and TCP-position sensitivity [32].

These measures describe different properties and use different units. They are first normalized using percentiles, with the preferred direction of each measure taken into account. The normalized measures are then combined with equal weights into a composite-quality index. This gives a single score for comparing their combined characteristics. The upper nominal 10% of the composite-quality distribution is retained as the high-quality workspace subset. These configurations have relatively favorable combined kinematic, payload-loading, and positioning-sensitivity characteristics.

A separate multi-objective dominance screening is also applied to the workspace measures [15]. Instead of combining the measures into one score, this method retains configurations that offer different advantages across the individual measures. The composite-quality ranking and the dominance screening are two parallel classification methods. Their retained subsets can overlap; one is not produced by further filtering the other. The screened-Pareto subset is the result of the adopted screening procedure, not a proven exact Pareto frontier for every sampled configuration. Section 6 compares both subsets with the full sampled population.

3.5 Candidate trajectory generation

Trajectory generation begins with a prescribed sequence of Cartesian positions and orientations. The procedure is general and does not depend on a particular demonstration shape. Multiple inverse-kinematic starting guesses, or seeds, are used to find different joint-space paths for the same Cartesian task.

At each prescribed pose, inverse kinematics finds joint configurations that satisfy the pose and joint-limit requirements. Solutions are then followed from one pose to the next using starting guesses that favor continuity. This avoids choosing only one inverse-kinematic branch before the alternatives have been examined. Successive configurations are connected only when they satisfy the specified joint-space continuity requirements. The resulting candidate paths are intended to avoid large jumps between incompatible inverse-kinematic branches.

These candidate trajectories are generated independently of the high-quality and screened-Pareto workspace classifications. In particular, the trajectory seeds do not result from successively reducing those workspace subsets. Their membership in the preferred workspace subsets is checked afterward. This makes it possible to compare the quality of an individual starting configuration with the feasibility of the entire path. Each retained joint path is an alternative way to perform the Cartesian task. The paths are carried forward for dynamic and workspace-aware evaluation instead of being ranked only by their starting configurations [11].

3.6 Inverse kinematics, continuity and timing

The desired Cartesian pose path is written as

$$\{p_d(u), R_d(u)\}, \qquad u \in [0,1], \tag{15}$$

where $p_d(u)$ and $R_d(u)$ are the desired TCP position and orientation, and u identifies progress along the path.

Inverse kinematics finds joint configurations whose forward-kinematic pose approximately matches the desired pose [11]:

$${}^0T_6(q) \approx {}^0T_{6,d}. \tag{16}$$

Continuity is examined using the change between consecutive joint configurations:

$$\Delta q_k = q_{k+1} - q_k, \tag{17}$$

where q_k and q_{k+1} are neighboring configurations along a candidate path. A large isolated change may indicate a jump between incompatible inverse-kinematic branches. Such branch-scale jumps are rejected rather than treated as acceptable physical motion. Passing the joint-space continuity check is not sufficient by itself. Interpolation between the original samples may still produce unacceptable TCP position or orientation errors. Therefore, continuous candidate paths are checked again at densely sampled points against the prescribed Cartesian full-pose tolerances before dynamic evaluation.

All accepted candidates use the same duration, $T = 6$ s, and a consistent timing convention. For a smooth timing law $u(t)$, joint velocity is

$$\dot{q} = \frac{dq}{du}\dot{u}, \tag{18}$$

and joint acceleration is

$$\ddot{q} = \frac{d^2q}{du^2}\dot{u}^2 + \frac{dq}{du}\ddot{u}. \tag{19}$$

These equations show how the joint-space path and the timing law together determine joint velocity and acceleration. Thus, path construction and timing can be described separately while preserving the required Cartesian position and orientation [16]. The common duration and timing convention allow the accepted trajectories to be compared consistently in Section 4.

4 Workspace-Aware Trajectory Optimization

Section 3 described the workspace and generated alternative joint-space paths for the same Cartesian task. This section compares the accepted paths using the robot's required joint torques and mechanical work. Workspace-quality measures are retained to help interpret the results.

The aim is not to choose a single path by assigning weights to different objectives. Instead, the method retains trajectories that represent useful trade-offs for later actuator selection and closed-loop testing. At this stage, the dynamic calculations use the robot-side model; motor, gearbox, and electrical-drive models are introduced in Section 5. The four-objective Pareto comparison does not directly include the workspace-quality measures.

4.1 Candidate lineage and continuity-preserving evaluation

The multi-seed inverse-kinematic method in Section 3.5 generates several joint-space paths for the same task. Each path keeps its original identifier C_k, where k is the source-candidate number. This label allows a candidate to be followed through later screening and evaluation; it is not a performance rank.

Before calculating dynamic performance, the joint-space continuity of each candidate is checked. The size of the change between neighboring joint configurations is

$$d_k = \|\mathbf{q}_{k+1} - \mathbf{q}_k\|_2 . \tag{20}$$

A large isolated d_k can indicate a jump between incompatible inverse-kinematic branches rather than a continuous robot motion. The screening method uses the observed separation between the maximum joint increments of continuous and discontinuous paths. Percentile-based jump ratios provide additional diagnostic information.

Paths that pass this test are represented by piecewise cubic interpolation. Their interpolated motion is then checked at many closely spaced points to confirm that both TCP position and orientation remain within the prescribed tolerances between the original samples. Only paths that pass both the continuity and dense full-pose checks are used for dynamic evaluation. All

accepted paths have the same duration, $T = 6$ s, and use a consistent timing convention. Section 6 reports how many candidates pass each screening stage.

4.2 Robot-side dynamic objectives

For each accepted trajectory, the joint torques required to perform the motion are calculated from the robot dynamics in Eq. (1):

$$\boldsymbol{\tau}_{\text{req}}(t) = \mathbf{M}(\mathbf{q})\ddot{\mathbf{q}} + \mathbf{c}(\mathbf{q}, \dot{\mathbf{q}}) + \mathbf{g}_q(\mathbf{q}) + \boldsymbol{\tau}_f(\dot{\mathbf{q}}). \tag{21}$$

Four objectives are used to compare the mechanical demands of the trajectories. Two describe joint-torque demand, and two describe mechanical work. Define $\tau_N(t) = \|\boldsymbol{\tau}_{\text{req}}(t)\|_2$ as the magnitude of the complete six-joint torque vector, and $P_j(t) = \tau_j(t)\dot{q}_j(t)$ as the mechanical power at joint j.

All four objectives are minimized:

$$f_1 = \max_t \tau_N(t), \qquad f_2 = \sqrt{\frac{1}{T}\int_0^T \tau_N^2(t)\, dt}, \tag{22}$$

$$f_3 = \sum_{j=1}^{6} \int_0^T \max(P_j(t), 0)\, dt, \quad f_4 = \sum_{j=1}^{6} \int_0^T |P_j(t)|\, dt. \tag{23}$$

The first objective, f_1, is the largest aggregate joint-torque demand during the motion. The second, f_2, is the root-mean-square (RMS) aggregate torque demand over the full trajectory. Both use the magnitude of the six-joint torque vector, not the torque of only one joint. The third objective, f_3, adds the positive mechanical work at the robot joints. The fourth, f_4, adds the magnitudes of both positive and negative mechanical work. These are robot-side mechanical quantities, not electrical-energy consumption: motor and inverter losses and regenerative efficiency are not included.

A path with a smaller peak torque may still require greater RMS torque or mechanical work. Keeping the four objectives separate makes these trade-offs visible. Joint travel, Cartesian pose error, acceleration, and workspace-quality measures are used for screening and interpretation, but they are not additional objectives in this dynamic Pareto comparison.

4.3 Pareto dominance and representative trajectories

The accepted paths are compared using the four objectives in Eqs. (22) and (23). A trajectory may perform better in one objective and worse in another [33]. Multi-objective optimization allows these competing alternatives to be retained [18, 34, 35]. The objectives are not combined into a weighted sum. Such a sum would require choosing relative preferences among quantities with different meanings and units. In addition, a weighted-sum approach may miss some nondominated solutions in a nonconvex objective space [18, 34].

For minimization, trajectory a dominates trajectory b if a is no worse in every objective and is strictly better in at least one. Mathematically, for f_i, $i = 1, \ldots, 4$, this is written as

$$\begin{aligned} &f_i(a) \le f_i(b), \quad \forall i, \\ &f_i(a) < f_i(b), \quad \text{for at least one } i. \end{aligned} \tag{24}$$

The dominance relation is denoted by $a \prec b$. A candidate is nondominated if no other evaluated candidate dominates it. The nondominated set is

$$\mathcal{P} = \{c : \nexists\, b \text{ such that } b \prec c\}. \tag{25}$$

These definitions follow standard Pareto principles [18, 19, 34, 35].

The dominance rule is applied only to candidates that have passed both joint-space continuity and dense Cartesian full-pose checks. The resulting set is therefore nondominated among the evaluated candidates. It is not claimed to be globally optimal among all possible robot trajectories. Original candidate labels are kept throughout the process. For example, C3 and C24 mean source candidates 3 and 24; the numbers are not ranks. Different representatives can be selected from the nondominated set according to their strengths, such as lower peak torque, lower RMS torque, or lower mechanical work [18, 34]. No single representative is automatically best for every objective.

Workspace-quality measures from Section 3 are then used to interpret the dynamically favorable paths. They help identify whether a path passes through configurations with poor local dexterity or unfavorable payload or TCP-position sensitivity. These measures provide additional context; they do not enter the four-objective dominance calculation. The retained representatives are carried forward for motor–gearbox sizing and closed-loop validation. Section 6.1.3 reports the selected candidates and the specific results for C3 and C24.

5 Actuator and Electromechanical Model

Section 4 identifies joint-space trajectories that differ in required torque and mechanical work. This section uses those requirements to select motor–gearbox combinations and examine how they perform in an electromechanical simulation. Instead of considering only the largest torque value, the selection uses each joint's torque, velocity, and acceleration throughout the motion. Candidate motors and gearboxes are checked against manufacturer limits at each joint. The feasible choices are then combined into complete six-joint actuator architectures and compared using system-level measures. Finally, the selected architecture is evaluated using a permanent-magnet synchronous motor (PMSM) model with field-oriented control (FOC) and computed-torque control (CTC). C3 and C24 are compared using the same actuator architecture and controller settings. This ensures that differences within

this comparison are not caused by changing the hardware or retuning the controller.

5.1 Actuator Requirements from the Retained Pareto Trajectories

For each retained trajectory, the robot-side joint-torque demand is calculated from the rigid-body model in Section 2:

$$\boldsymbol{\tau}_{\text{req}} = \mathbf{M}(\mathbf{q})\ddot{\mathbf{q}} + \mathbf{c}(\mathbf{q}, \dot{\mathbf{q}}) + \mathbf{g}_q(\mathbf{q}) + \boldsymbol{\tau}_f(\dot{\mathbf{q}}). \tag{26}$$

For each joint, actuator screening examines the torque, velocity, and acceleration over the entire trajectory. A single static-load value or maximum torque value cannot describe all these demands. The two retained trajectories also place different demands on the actuators. C3 has the lower peak aggregate joint torque, while C24 has lower root-mean-square (RMS) aggregate torque and lower mechanical-work objectives. Therefore, a motor–gearbox combination is accepted only if it meets the requirements of both trajectories.

For a reduction ratio N_j and gearbox efficiency η, motor speed and delivered joint torque satisfy

$$\omega_{m,j} = N_j \dot{q}_j, \qquad \tau_{d,j} = \eta N_j T_{e,j}. \tag{27}$$

Here $\omega_{m,j}$ is the motor speed, $T_{e,j}$ is the electromagnetic torque produced by the motor, and $\tau_{d,j}$ is the torque delivered to the joint through the gearbox. When the gear ratio is constant, motor acceleration equals $N_j \ddot{q}_j$. Equation (27) describes how the gearbox changes speed and transmitted torque. The additional torque needed to accelerate the motor rotor is considered separately through reflected inertia in Sections 5.2 and 5.5.

5.2 Gear-Ratio Search and Joint-Level Feasibility

The motor and gearbox reduction ratio are selected together because each affects the suitability of the other. For a given joint load, a larger reduction ratio generally allows the motor to produce less torque. However, it also requires the motor to rotate and accelerate faster. In addition, it increases the motor rotor inertia as seen from the robot joint:

$$J_{\text{ref},j} = J_{m,j} N_j^2, \tag{28}$$

where $J_{m,j}$ is the inertia of the motor rotor. Thus, increasing the gear ratio can help transmit the required torque but also increases the effective inertia that must be accelerated. Selecting a suitable ratio therefore requires balancing torque capacity, motor speed, reflected inertia, gearbox ratings, and the remaining operating reserve.

The search tests available manufacturer motor–gearbox combinations and reduction ratios against both retained trajectories. For each joint, it checks peak and continuous motor-torque ratings, maximum motor speed, gearbox torque and input-speed limits, and the specified mechanical safety margins. A combination is rejected if it fails any required check for either trajectory. The continuous-torque check provides an initial assessment of sustained loading, but it does not prove that the motor can operate repeatedly without overheating. Motor voltage and current are evaluated later with the PMSM–FOC model; they cannot be determined from mechanical ratings alone.

Only motor–gearbox combinations that pass the joint-level checks are used to build complete six-axis architectures. Thus, actuator selection is based on more than gravity loading at rest or the maximum torque of one trajectory.

5.3 Six-Joint Architecture Construction and Pareto Selection

Each joint may have several feasible motor–gearbox choices. Combining these choices produces different possible designs for the complete six-joint robot. One such actuator architecture is written as

$$\mathcal{A} = \{(M_1, N_1), \ldots, (M_6, N_6)\}, \tag{29}$$

where M_j identifies the motor–gearbox choice for joint j and N_j is the corresponding reduction ratio.

Choosing the most powerful actuator for every joint is not necessarily the best system-level design. It may make the robot heavier or larger and increase reflected inertia. Therefore, the six actuators are evaluated together [3]. First, joint-level choices that are dominated by other choices are removed to reduce the number of combinations [18]. The remaining choices are combined using exact Pareto propagation. The resulting architectures are compared by total actuator mass, total and worst-joint reflected rotor inertia, a measure of motor size (motor envelope), and the minimum robustness margin across the architecture.

These measures involve trade-offs. For example, a design with more available torque may also have greater mass or inertia. Instead of combining the measures into one weighted score, the method retains architectures that are not dominated by other evaluated designs [19]. This preserves alternatives with different strengths. The aim is not simply to choose the largest actuators, but to find a feasible combination that balances available capacity against mass, size, and inertia. Section 6 reports how the search space is reduced and which architecture is selected for simulation.

5.4 PMSM Electrical Model and Field-Oriented Control

Passing the mechanical checks does not guarantee that a motor can produce the required torque without exceeding its electrical limits. To examine this, the selected architecture is simulated using the following surface-mounted PMSM model [36]:

$$v_d = R_s i_d + L_d \dot{i}_d - \omega_e L_q i_q, \tag{30}$$

$$v_q = R_s i_q + L_q \dot{i}_q + \omega_e (L_d i_d + \lambda_m), \tag{31}$$

with electromagnetic torque

$$T_e = \frac{3}{2} p \lambda_m i_q, \tag{32}$$

for $L_d = L_q$ and $i_d^* = 0$. Here v_d and v_q are the direct- and quadrature-axis voltages; i_d and i_q are the corresponding currents; R_s is stator resistance; L_d and L_q are the axis inductances; ω_e is electrical angular speed; λ_m is permanent-magnet flux linkage; and p is the number of pole pairs.

The adopted FOC strategy keeps the reference direct-axis current at zero, $i_d^* = 0$, and controls i_q to produce the requested motor torque [37]. Therefore, a motor that passes the mechanical checks may still be unsuitable if the required current or voltage exceeds the available electrical limits.

The DC-link voltage is $V_{\mathrm{dc}} = 48$ V. With the adopted space-vector pulse-width modulation (SVPWM) utilization factor of 0.95, the available peak dq-voltage magnitude is

$$V_{\max} = 0.95 \frac{48}{\sqrt{3}} = 26.3272 \text{ V}. \tag{33}$$

The current controllers are designed for a 1-kHz bandwidth. Their proportional and integral gains are $K_{p,i} = L\omega_c$ and $K_{i,i} = R_s \omega_c$, respectively. Here ω_c is the design angular bandwidth and L is the inductance of the relevant axis. Field weakening, which could extend operation beyond the usual voltage-limited speed range, is not used. The electrical simulation therefore checks whether the requested motion can be achieved within the modeled current and voltage limits.

5.5 Inertia-Consistent CTC and Multi-Rate Validation

The reflected rotor inertia in Eq. (28) is included consistently in the simulated mechanical plant and the computed-torque model. The augmented joint-space inertia matrix is

$$\mathbf{M}_a(\mathbf{q}) = \mathbf{M}(\mathbf{q}) + \mathrm{diag}\left(J_{\mathrm{ref},1}, \ldots, J_{\mathrm{ref},6}\right). \tag{34}$$

Using the same augmented inertia in the mechanical plant and controller model prevents an inconsistency in which motor inertia affects the simulated robot but is ignored by the controller.

The CTC law combines model-based compensation with proportional–derivative tracking feedback [38]:

$$\begin{aligned} \boldsymbol{\tau}_c = \mathbf{M}_a(\mathbf{q}) \left[\ddot{\mathbf{q}}_d + \mathbf{K}_d(\dot{\mathbf{q}}_d - \dot{\mathbf{q}}) + \mathbf{K}_p(\mathbf{q}_d - \mathbf{q})\right] \\ + \mathbf{c}(\mathbf{q}, \dot{\mathbf{q}}) + \mathbf{g}_q(\mathbf{q}) + \boldsymbol{\tau}_f(\dot{\mathbf{q}}), \end{aligned} \tag{35}$$

where $\mathbf{q}_d$, $\dot{\mathbf{q}}_d$, and $\ddot{\mathbf{q}}_d$ are the desired joint trajectories, and $\mathbf{K}_p$ and $\mathbf{K}_d$ are the position- and velocity-error gain matrices. The controller computes the joint torque needed to follow the reference while compensating for the modeled dynamics. The gain values used in the reported scenario comparisons are specified in Section 6.2. C3 and C24 are tested with the same actuator architecture and controller configuration. As a result, their comparison is not affected by changes in hardware or controller gains.

The coupled robot–gearbox–PMSM–FOC–CTC simulation uses different update rates for different parts of the system [39]. The mechanical plant and electrical equations are integrated every 25 μs. The motor current controller is updated every 50 μs, while the outer trajectory and CTC controller are updated every 6 ms. Cartesian tracking is compared at the common 6-ms sampling times. The faster signals are also retained so that short-duration peaks in motor, inverter, and actuator demands can be checked.

The complete task-to-actuator sequence is summarized as

$$\begin{array}{l} \text{Pareto trajectories} \\ \quad \downarrow \\ \text{joint dynamic demands} \\ \quad \downarrow \\ \text{motor–gear–ratio search} \\ \quad \downarrow \\ \text{architecture Pareto set} \\ \quad \downarrow \\ \text{PMSM–FOC–CTC validation.} \end{array} \tag{36}$$

The final simulation checks whether the selected trajectories and actuator architecture remain feasible when gearbox effects, motor electrical behavior, controller action, and operating limits are included. Its results describe performance under the specified simulated task and operating conditions. They do not prove that the system is suitable for repeated thermal loading or that it will achieve the same performance on a physical robot.

The preceding sections introduced measures for workspace geometry, motion capability, robot dynamics, actuator selection, and closed-loop tracking. Each serves a different purpose. Table 1 summarizes what these quantities mean and how they influence design decisions. It also provides a guide for interpreting the results in the next section.

6 Results and Discussion

This section follows the main stages of the proposed framework: workspace analysis, trajectory screening, dynamic Pareto evaluation, actuator selection, and closed-loop validation. The workspace and initial trajectory studies identify possible robot configurations and alternative joint motions. A separate experiment then compares four letter-E trajectories to examine how rounding corners and selecting optimized trajectories affect Cartesian tracking. The letter E contains straight segments, changes in direction, and a reversal. These features make it useful for examining tracking near changes in path geometry. The original trajectory benchmark has not been shown to be identical to the later letter-E reference. For this reason, the two experimental stages are discussed separately.

Table 1: Principal quantities in the integrated task-to-actuator framework.

Analysis area	Quantity / measure	Physical meaning	Influence on design / interpretation
Workspace	Spatial bounds (x, y, z)	Sampled TCP positions extents	Defines sampled workspace limits.
	Radial reach	TCP distance from robot base	Characterizes manipulator reach.
	Convex-hull volume	TCP positions outer envelope	Summarizes extent of workspace.
Workspace quality	$\sigma_{\min}$	The least singular value of J_v	Low $\sigma_{\min}$ indicates proximity to a translational singularity.
	μ_v	Translational manipulability	Low μ_v indicates reduced translational dexterity.
	κ_v	Jacobian condition number	Large κ_v indicates poor conditioning.
	Payload-induced torque	Additional payload joint loading	Distinguishes loading limits from geometric reach.
	Payload-sensitivity norm	Torque change per unit payload	Shows payload-sensitive configurations.
	$\|\delta p\|$ for prescribed δq	Joint-error-to-TCP sensitivity	Shows position-sensitive configurations.
	Composite-quality index	Normalized workspace metrics	Identifies high-quality workspace regions.
	Screened workspace-Pareto subset	Configurations retained by screening	Retains alternative workspace-quality trade-offs.
Trajectory generation	IK feasibility	Pose and joint-limit satisfaction	Removes infeasible configurations.
	Δq_k, d_k	Inter-sample joint displacement	Detects branch discontinuities.
	Joint travel	Accumulated joint displacement	Measures joint-space motion economy.
Robot dynamics	$f_1 = \max_t \|\tau_{\text{req}}(t)\|_2$	Peak aggregate torque	Minimizes worst-case dynamic loading.
	$f_2 = \text{RMS}\{\|\tau_{\text{req}}(t)\|_2\}$	Sustained aggregate torque	Minimizes sustained torque loading.
	f_3	Positive mechanical work	Measures positive work demand.
	f_4	Absolute mechanical work	Measures total bidirectional work.
	Dynamic Pareto set $\mathcal{P}$	Nondominated trajectories	Preserves dynamic trade-offs.
Workspace-aware evaluation	$f_{\text{traj}}(\chi)$	Trajectory-performance descriptors	Characterizes path-level performance.
	$f_{\text{ws}}(\chi)$	Path-sampled workspace descriptors	Identifies unfavorable workspace exposure.
	Path-level comparison	Dynamic results with workspace descriptors	Supports interpretation; not an additional Pareto objective.
Actuator design	Motor–gearbox choice M_j	Motor–gearbox selection	Determines actuator characteristics.
	Gear ratio N_j	Transmission reduction ratio	Trades torque, speed, and inertia.
	Gearbox efficiency η	Transmission efficiency	Relates motor and delivered joint torque.
	ρ_j	Capacity-to-demand ratio	Measures worst joint-level reserve.
	Continuous motor torque	Continuous torque capability	Screens sustained-duty loading.
	Peak motor torque	Transient torque capability	Enforces peak-torque feasibility.
	Gearbox torque / input speed	Transmission capacity limits	Prevents gearbox overload.
Electrical drive	i_d, i_q	Direct- and quadrature-axis currents	Produces torque with $i_d^* = 0$.
	Motor current rating	Permissible current demand	Screens electrical loading.
	$V_{\max} = 26.3272$ V	Available peak dq voltage	Enforces voltage feasibility.
	$V_{\text{dc}} = 48$ V	DC-link voltage	Defines inverter voltage availability.
Closed-loop validation	Reflected inertia J_{ref}	Joint-referred motor inertia	Ensures plant–controller consistency.
	Cartesian RMSE	RMS TCP-position error	Measures overall tracking accuracy.
	Cartesian MAE	Mean absolute TCP error	Measures average tracking deviation.
	Maximum Cartesian error	Peak TCP-position error	Measures worst-case tracking error.
	Peak-torque compliance	Peak torque versus allowable limit	Verifies closed-loop torque feasibility.
	Voltage compliance	Voltage demand versus $V_{\max}$	Checks modeled voltage-limit compliance.
	Continuous-rating excursions	Time above continuous rating	Flags potential thermal-duty concerns.

6.1 Workspace, Trajectory, and Electromechanical Results

6.1.1 Workspace Characterization and Dynamic Capability

The workspace analysis examined 50,000 joint configurations. Each configuration represents one robot posture, not a complete trajectory. The sampled frame-6 TCP positions covered $x \in [-1.059742, 1.075896]$ m, $y \in [-1.056034, 1.049982]$ m, and $z \in [-0.844823, 1.276308]$ m. The sampled radial reach ranged from 0.044223 to 1.295706 m, with a mean of 0.661485 m and a median of 0.653378 m. The convex hull enclosing the sampled positions had a volume of 4.978539 m^3, as shown in Fig. 2(a). This volume describes an outer envelope, not a region that is necessarily fully reachable, collision-free, or equally suitable for motion. In particular, the convex hull may cover gaps and non-convex boundaries within the actual workspace.

The sampled positions also differed greatly in local motion capability, as shown in Fig. 2(b). The smallest sampled singular value of the translational Jacobian was 1.5207×10^{-3} m, and its median was 0.185154 m. Median translational manipulability was 0.054636 m^3. The median Jacobian condition number was 3.8703, while the largest finite sampled value was 418.51. None of the randomly sampled configurations fell below the chosen near-singularity threshold of 10^{-3} m. However, a targeted numerical search found a much smaller singular value of 4.41×10^{-17} m. This result shows that random sampling can describe general workspace behavior but still miss a small region close to a singularity. Therefore, a position being reachable or lying

inside the convex hull does not guarantee good kinematic conditioning.

Payload loading and sensitivity to joint-position errors provide further information about reachable configurations. With the 18-kg payload, the largest sampled gravity torque from the robot and payload occurred at J2 and was 408.09 N m. The payload alone contributed approximately 210.28 N m at J2, giving a peak payload sensitivity of 11.682 N m/kg. Adding a payload changes the torque required and the remaining actuator reserve, but not the geometric reach of a robot with fixed geometry and joint limits. Assuming independent joint-position uncertainty of 1 arcmin, the median calculated TCP-position sensitivity was 0.2543 mm and the largest sampled value was 0.4747 mm. These values are model-based predictions, not measurements of robot repeatability.

The 50,000 sampled configurations were classified in *two separate but overlapping ways*. A composite-quality score placed 5,001 configurations in the upper nominal 10% group. A separate multiobjective screening retained 1,094 screened workspace-Pareto configurations, or approximately 2.19% of the original sample. The composite score combines several favorable properties into one ranking. In contrast, Pareto screening retains configurations that offer different trade-offs among those properties. The membership check found 686 configurations in *both* groups, 4,315 only in the high-quality group, 408 only in the screened-Pareto group, and 44,591 in neither. Thus, 686 of the 1,094 screened-Pareto configurations also belonged to the high-quality group. The 1,094 configurations form a *screened* Pareto population.

Figure 3(a) shows where the two groups occur in the sampled workspace. Figure 3(b) shows the trade-off between distance from translational singularity and payload sensitivity, together with the composite-quality score. Because the groups overlap only partly, neither classification replaces the other. A single quality score can hide configurations that perform well on one particular measure, while Pareto membership alone does not reproduce the composite ranking. The counts of 5,001 and 1,094 refer to *individual configurations*, not complete trajectories. They are not successive filtering stages that produce the 24 trajectories considered below.

6.1.2 Candidate Joint-Space Realizations and the Letter-E Demonstration

The workspace results above describe individual robot postures. Completing a Cartesian task, however, requires an *ordered sequence* of joint configurations that produces the desired motion. Therefore, the 50,000 configurations, the two workspace groups, and the trajectory candidates must not be treated as one sequence of numerical reductions. The initial archived Stage-3 study generated 24 candidate joint-space paths using different inverse-kinematics seeds. The paths were labeled C1–C24, and each initially contained 301 joint-position samples. These labels identify candidates, not their rankings. The original Cartesian benchmark has not been established as identical to the later letter-E reference. The letter-E experiment is discussed separately in Section 6.2.

Table 2: Selected workspace and sensitivity results.

Quantity	Value
Workspace samples	50,000
Convex-hull outer-envelope volume	4.978539 m^3
Reach min / max	0.044223 / 1.295706 m
Median σ_{min}	0.185154 m
Minimum random-sample σ_{min}	1.5207×10^{-3} m
Refined minimum σ_{min}	4.41×10^{-17} m
Median manipulability	0.054636 m^3
Median condition number	3.8703
Top-10% composite-quality samples	5,001
Screened workspace Pareto samples	1,094
TCP sensitivity, 1 arcmin: median / peak	0.2543 / 0.4747 mm

Comparing the trajectory seeds with the workspace groups gives an important result. Only four of the 24 seeds belonged to the 5,001-member high-quality group: C3, C17, C23, and C24. Only C3 belonged to the 1,094-member screened workspace-Pareto group. Eighteen seeds belonged to a broader preliminary workspace-Pareto candidate mask, which is *different* from the final 1,094-member screened group. Thus, the 24 paths were not generated by choosing 24 configurations from the screened-Pareto group or by selecting the 24 highest composite scores. This is because the letter E is not expected to cover the entire robot reach and a promising initial posture does not, by itself, establish that the complete trajectory will be suitable.

The next test checked whether each candidate followed a continuous joint-space path. Eleven of the 24 candidates passed: C1, C3, C5, C7, C8, C13, C14, C16, C17, C19, and C24. The other 13 candidates (C2, C4, C6, C9–C12, C15, C18, and C20–C23) contained branch discontinuities. In the corrected archive, the largest maximum joint-position step among the accepted paths was 0.059067 rad. Even the smallest maximum step among the rejected paths was approximately 4.6084 rad. This large difference indicates abrupt changes between inverse-kinematic branches, not merely small differences in workspace quality. For example, C23 started from a high-quality configuration but failed the continuity test.

The 11 continuous paths were then checked at more closely spaced points along the complete Cartesian pose. Eight paths satisfied both maximum-error limits: 0.1 mm for position and 0.1° for orientation. These were C3, C5, C13, C14, C16, C17, C19, and C24. The other three failed the dense-pose test: C1 exceeded the orientation limit (0.10362°), C7 exceeded the position limit (0.11072 mm), and C8 exceeded the orientation limit (0.11581°). These relatively small pose errors differ from the large joint-space jumps that caused the first 13 rejections. The result also shows why checking only the original IK samples and joint continuity is



(a) (b)

Figure 2: Complementary views of the sampled geometric workspace: (a) the convex-hull outer envelope used to compute the 4.978539 m^3 enclosing volume, and (b) the same sampled workspace colored by the translational Jacobian minimum singular value. The convex hull is an outer-envelope approximation rather than the exact usable workspace, whereas panel (b) exposes the variation in local kinematic quality within the reachable set.



(a) (b)

Figure 3: Multi-metric workspace-quality screening: (a) sampled workspace with the top-10% composite-quality subset and screened workspace-Pareto subset; and (b) the trade-off between translational singularity margin and payload sensitivity, with color denoting the composite-quality index and outlined points denoting the screened workspace-Pareto set. Together the panels show that geometric reachability alone does not identify the configurations with the most favorable combined kinematic, loading, and positioning-sensitivity characteristics.

not enough to guarantee accuracy between samples.

The initial trajectory seeds were chosen independently of the Stage-2 high-quality and screened-Pareto classifications. They came from workspace configurations near the starting Cartesian pose and from other joint-space alternatives. Their membership in the two workspace groups was checked *after* generation. Most seeds therefore fell outside the preferred groups without contradicting the workspace analysis. Stage 2 evaluated the local properties of individual configurations, including dexterity, payload sensitivity, and joint-error-to-TCP sensitivity. Stage 3 evaluated complete paths for continuity and full-pose accuracy. C23 demonstrates that a high-quality starting configuration does not guarantee an acceptable trajectory. Conversely, C5, C13, C14, C16, and C19 passed both path checks even though their seeds belonged to neither preferred workspace group. Favorable local classification was therefore neither necessary nor sufficient for trajectory acceptance. Workspace analysis helped explain the candidates; it did not act as an exclusive filter for generating them.

In summary, screening reduced the *24 generated paths* to *11 continuous paths* and then to *eight paths meeting dense full-pose accuracy requirements*. Candidate labels were preserved throughout. The refined accepted trajectories all have a duration of 6 s.

6.1.3 Trajectory-Level Pareto Results: Origin and Meaning of C3 and C24

The four objectives in Eqs. (22) and (23) were calculated for each of the eight accepted trajectories. Applying the dominance rule in Eq. (24) retained two non-dominated candidates: C3 and C24. Their labels refer to the original IK candidates. Their objective values, rather than their label numbers, explain why both were retained.

C3 had the lowest peak aggregate torque norm,

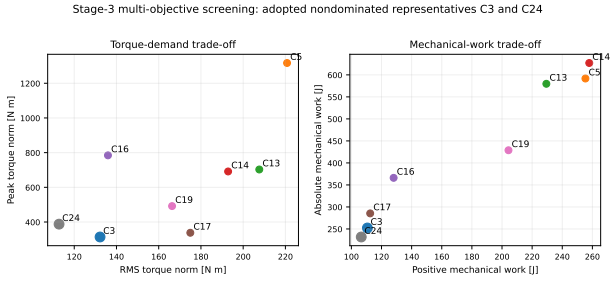


Figure 4: Multi-objective trade-offs reconstructed from the adopted candidate arrays. C3 and C24 are the two retained nondominated representatives.

Table 3: Adopted Stage-3 Pareto representatives.

Objective	C3	C24
Peak torque norm [N m]	313.605	387.635
RMS torque norm [N m]	132.223	112.812
Positive mechanical work [J]	110.623	106.554
Absolute mechanical work [J]	252.196	231.766

$f_1 = 313.605$ N m. Its RMS torque norm was 132.223 N m, its positive mechanical work was 110.623 J, and its absolute mechanical work was 252.196 J. C24 had a higher peak aggregate torque norm of 387.635 N m, but lower RMS torque (112.812 N m), positive work (106.554 J), and absolute work (231.766 J). Thus, C3 favors a lower *peak torque demand*, while C24 favors lower *sustained torque and mechanical work*. Although C24 has lower values in three objectives, C3 remains better in peak torque. Neither dominates the other, and the number of objectives won does not identify one universally best trajectory. The later C/D experiment compares optimized trajectories associated with these candidates under common hardware and control settings. It does not claim byte-for-byte identity between all historical candidate files and the later simulation references.

Both candidates perform the same Cartesian task in the same amount of time, but they distribute joint motion and dynamic loading differently. They are therefore carried through the same actuator-selection procedure and later evaluated with the same controller. This makes it possible to examine whether the Pareto trade-off remains important after motor, gearbox, and closed-loop dynamics are considered.

Figure 4 illustrates the trade-off: C3 has the lower peak torque demand, while C24 has lower RMS torque and both mechanical-work measures.

6.1.4 Motor–Gearbox Search and Architecture Pareto Results: Origin and Meaning of A218

The torque and motion demands of C3 and C24 were used in the manufacturer-constrained search described in Sections 5.1–5.3. At each joint, motor–gearbox–ratio combinations had to meet the selected mechanical margin for *both* trajectories. Exact local dominance screening then removed choices that could not improve the system-level objectives. Before this screening, the target-margin search contained 1,177,830,720 possible six-joint combinations. Local dominance reduced the number to 1,347,192. Exact Pareto propagation across the joints then produced 468 mechanically nondominated architectures. This staged procedure avoids detailed simulation of every possible combination by first removing mechanically inferior designs.

Each architecture surviving the system-level Pareto analysis received a permanent label A_k. As with trajectory labels, the number identifies the design rather than its performance rank: A218 means *architecture 218*. The Stage-5 search did not identify one architecture as best for every purpose. Instead, it retained representatives based on minimum total mass, total reflected inertia, largest individual-joint reflected inertia, motor-envelope proxy, largest minimum robustness margin, and a descriptive balanced distance from the normalized ideal point. These criteria produced four distinct representatives: A1, A192, A218, and A457. All four passed subsequent analytical electrical screening, with worst screening margins of 1.2136, 1.2927, 1.7083, and 2.0347, respectively. A218 was selected for detailed PMSM–FOC–CTC simulation and kept fixed for the C3/C24 comparison. It is therefore a selected representative of the mechanically nondominated designs, not the 218th-best architecture.

For A218, the reduction-ratio vector is written in a column-safe form as

$$\mathbf{N} = \begin{bmatrix} 80 & 160 & 160 & 160 & 160 & 50 \end{bmatrix}. \qquad (37)$$

The gearbox efficiency is $\eta = 0.85$. The selected motors are TBM2G-11526D at J1, TBM2G-09413D at J2, TBM2G-07613D at J3, and TBM2G-06013D at J4–J6. The corresponding joint-side continuous and peak capabilities are reported joint by joint in Table 4, avoiding an ambiguous long vector notation in the two-column layout.

The actuator ratings should not be interpreted simply as a ranking of gravity loads. Section 6.1.1 shows that J2 experienced the largest sampled gravity torque, yet A218 assigns higher continuous and peak ratings to J1. This is possible because actuator selection depends on the *complete* torque and speed histories for C3 and C24, as well as gear ratios, reflected inertia, manufacturer limits, robustness margins, and system-level Pareto objectives. For C3, the archived maximum absolute torques at J1 and J2 were 301.24 and 285.75 N m. For C24, they were 265.24 and 271.94 N m. Figure 5 compares these trajectory demands with the selected actuator capacities.

6.1.5 Electrical, Actuator and Closed-Loop Validation

The selected A218 architecture must be distinguished from the historical hypothetical enlarged H-A/H-B actuator configurations. H-A/H-B were counterfactual tests, not additional manufacturer-validated versions of A218. The original A218 was evaluated with the PMSM–FOC model in Section 5.4, using a 48-V DC bus and the 26.3272-V peak dq-voltage limit from

Table 4: Adopted A218 motor–gearbox architecture.

Joint	Motor	N	η	τ_{cont} [N m]	τ_{peak} [N m]
J1	TBM2G-11526D	80	.85	410.04	986.00
J2	TBM2G-09413D	160	.85	278.80	685.44
J3	TBM2G-07613D	160	.85	167.28	465.12
J4	TBM2G-06013D	160	.85	81.60	227.12
J5	TBM2G-06013D	160	.85	81.60	227.12
J6	TBM2G-06013D	50	.85	25.50	70.975

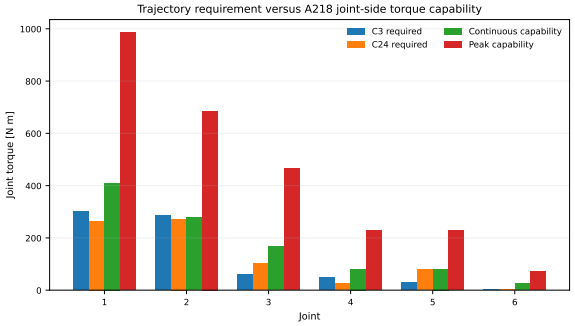


Figure 5: Archived C3/C24 robot-side peak joint-torque requirements compared with A218 continuous and peak joint-side capabilities.

Eq. (33). Historical actuator-level audits found that C3 and C24 satisfied the applicable hard peak-torque and voltage constraints. However, those checks do not prove full electrical feasibility for every later simulation using the G2 controller.

The results also identified short-duration demands above some continuous ratings. For C3, the continuous-torque utilization ratios at J1 and J2 were 1.04455 and 1.14519. For C24, the reported continuous-rating peak ratios at J2 and J5 were 1.19647 and 1.09996. Because these ratios were defined differently, their numerical values should not be treated as directly equivalent. A brief excursion above a continuous rating does not automatically violate a higher short-duration peak limit. Nevertheless, it may indicate a thermal concern during repeated operation. Since the simulated task lasts 6 s and the applicable hard peak limits were met, these excursions are reported as thermal-screening indicators rather than immediate peak-limit failures. Repeated-duty thermal suitability still requires a validated thermal model and repeated-cycle analysis. The actuator-level evidence therefore supports short-duration electromechanical feasibility under the common architecture, not thermal certification.

Current closed-loop tracking evidence. The Cartesian tracking results reported in this paper come from the a comparison. Section 6.2 and Table 5 present the four current results using the same sampling grid and explain which pairs allow controlled comparisons. Earlier controller results are not mixed into this table. The actuator-limit evidence discussed above comes from separate archived screening and must not be interpreted as a complete new electrical-feasibility audit of every current G2 run.

6.2 Four-Scenario Cartesian Tracking Comparison

A supplementary FC-ABCD-07 A11–N09 experiment compares four letter-E motions, each lasting 6 s. Scenario A follows the original sharp-corner path. Scenario B follows its rounded-corner version. Both use the hypothetical H1 actuator configuration and the G2 computed-torque controller. Scenarios C and D follow optimized rounded paths associated with C3 and C24, respectively, using the A218 actuator architecture and the same G2 controller. The C3/C24 associations follow the current simulation records.

Each simulation contained 240,001 joint-position samples at 25 μs intervals. These were evaluated on the common 6-ms controller grid, giving 1,001 samples. Forward kinematics to frame {6} reproduced the stored desired and actual Cartesian positions. The largest difference for the reference positions was zero; for actual positions, it was below 9×10^{-13} mm. Both records passed the reconstruction check. Although the records have the same model name, their joint-space references and outputs differ, confirming that they describe different motions. The C/D values below come from the separately reconstructed frame-6 arrays for the current G2/A218 comparison, rather than earlier Stage-6 tracking metrics.

Table 5 reports Cartesian position errors. At each time sample, the error is $e_k = \|p_d(t_k) - p(t_k)\|_2$. The root-mean-square error is RMSE $= \sqrt{\frac{1}{N}\sum_k e_k^2}$, the mean absolute error is MAE $= \frac{1}{N}\sum_k e_k$, and the maximum error is $e_{\max} = \max_k e_k$. All four cases use frame {6} and the same 6-ms grid. Under H1/G2, rounding the sharp-corner reference reduces RMSE from 44.5767 to 3.4071 mm, a 92.36% reduction. Maximum error falls from 264.5737 to 14.2799 mm, a 94.60% reduction. Figure 6 shows the paths, while Fig. 7 shows how the errors change over time.

With A218 Architecture and G2 controller gains held fixed, the optimized C24-associated trajectory gives a lower RMSE than the C3-associated trajectory: 1.7411 instead of 1.9781 mm, an improvement of 11.98%. Its maximum error is also lower: 2.4612 instead of 4.2737 mm, a reduction of 42.41%. These results show a difference in tracking between the optimized trajectories under the same actuator architecture and controller gains settings. However, the H1/G2 and A218/G2 groups use different actuator architectures. Differences between these groups therefore cannot be attributed to trajectory optimization alone. Moreover, small tracking errors do not prove that every torque, current, speed, voltage, or repeated-duty thermal limit is satisfied.

Figures 6 and 7 provide two views of the same tracking results. The three-dimensional paths show the large mismatch in sharp-corner Scenario A and the closer tracking in B, C, and D. The time plots show *when* the errors occur: A has a pronounced early transient, while B reaches its peak later. Under A218/G2, D has

Table 5: Current A11–N09 frame-6 Cartesian tracking results on the common 6-ms grid ($T = 6$ s, $N = 1001$). A/B numerical association was verified in P135; C/D values are from the separately reconstructed P118/P125 arrays. Architecture differs between the two controlled pairs.

Case	Reference geometry	Actuator / CTC	RMSE [mm]	MAE [mm]	Max [mm]	Comparison group
A	Original sharp-corner E	H1 / G2	44.5767	15.7690	264.5737	A versus B
B	Rounded-corner E	H1 / G2	3.4071	2.4757	14.2799	A versus B
C (C3)	Optimized rounded E	A218 / G2	1.9781	1.7921	4.2737	C versus D
D (C24)	Optimized rounded E	A218 / G2	1.7411	1.6535	2.4612	C versus D

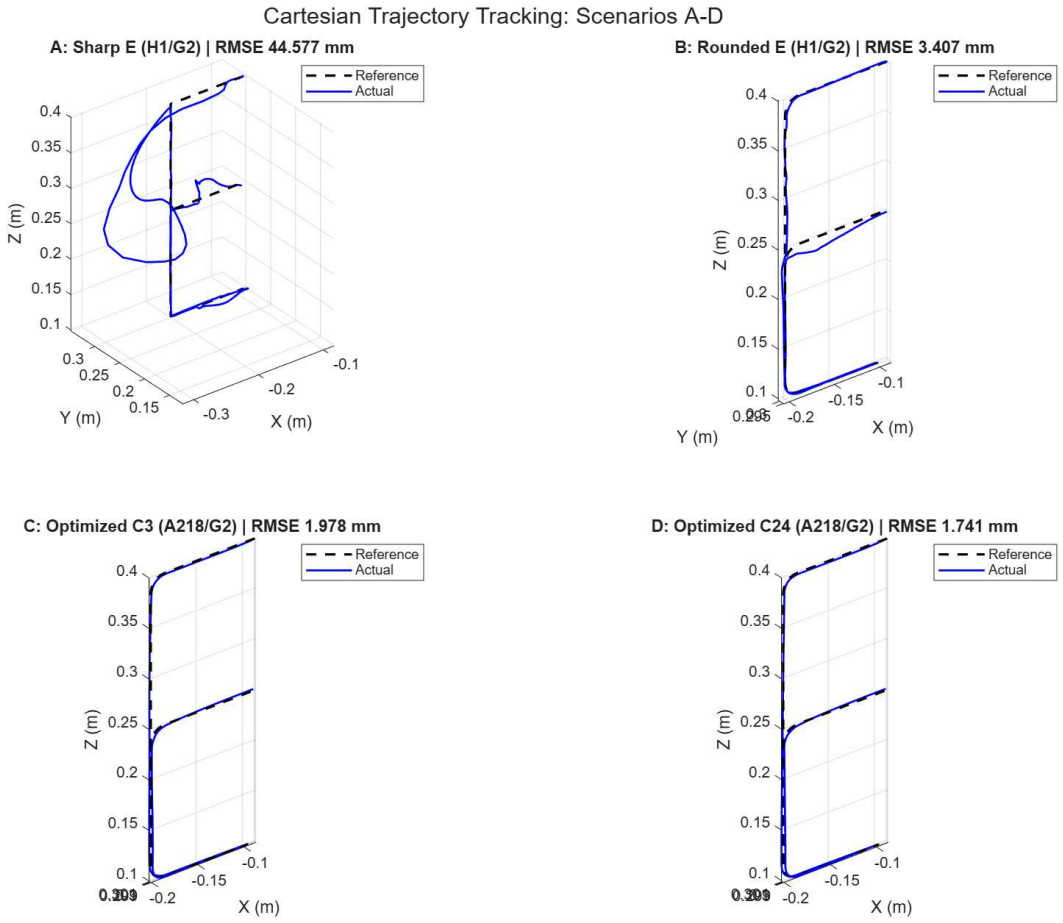


Figure 6: Frame-6 Cartesian reference (black dashed) and actual (blue solid) trajectories for (a) sharp E under H1/G2, (b) rounded E under H1/G2, (c) optimized C3 under A218/G2, and (d) optimized C24 under A218/G2. All results use the current A11–N09 data on the common 6-ms grid. Each panel uses an equal spatial aspect ratio; panel axes are independently displayed.

a lower peak error than C, as reported in the table. The plotted errors are magnitudes of the three-dimensional frame-6 position difference, not signed errors along individual axes. A particular error peak should not be assigned to a letter-E corner without matching its time to the corner location.

6.3 Integrated Task-to-Actuator Interpretation

Together, these findings support the integrated approach introduced in Section 1. First, the 4.978539-m^3 convex-hull volume describes an outer geometric envelope, not a guarantee of usable workspace. Dexterity, proximity to singularity, payload sensitivity, and TCP-position sensitivity vary across the reachable configurations. The targeted singularity search also shows that random sampling may miss small but important regions with poor kinematic conditioning.

Second, a Cartesian task can be completed by different joint-space trajectories with different dynamic demands. C3 favors lower peak aggregate torque, while C24 favors lower RMS torque and mechanical work. Keeping both Pareto alternatives avoids choosing a trajectory too early through a weighted score. Actuator selection adds another level of trade-offs. Local dominance reduced approximately 1.178×10^9 possible architectures to 1.347×10^6 before system-level Pareto propagation. This reduction shows why selecting a motor and gearbox separately for each joint is not enough. The final A218 gear ratios in Eq. (37) and motor ratings reflect complete-system trade-offs and need not follow

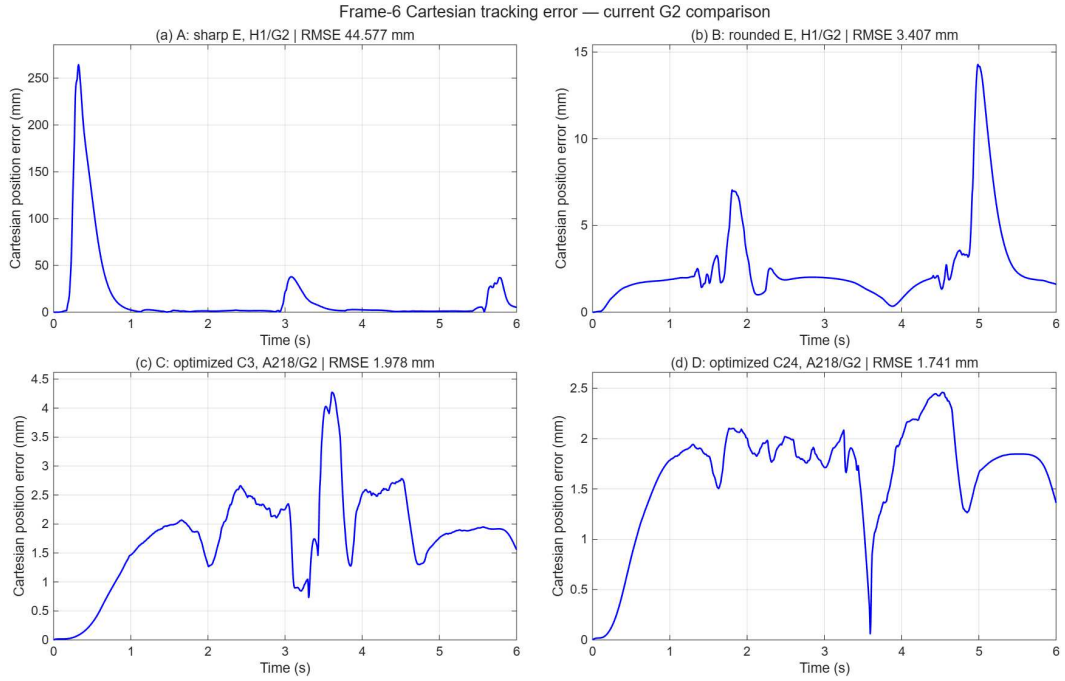


Figure 7: Frame-6 Cartesian position-error magnitude $e_p(t) = \|p_d(t) - p(t)\|_2$ for the current A11–N09 runs: (a) A, (b) B, (c) C, and (d) D. Panel-specific vertical scales reveal the different error histories; numerical metrics are compared in Table 5.

the ranking of gravity torque alone.

Finally, differences between the optimized trajectories remain visible after selecting the hardware and controller. With A218/G2 held fixed, D reduces RMSE by 11.98% and maximum Cartesian error by 42.41% relative to C. These results do not make C24 universally optimal or show that one objective alone caused the improvement. C24 differs in RMS torque, mechanical work, and the timing of joint demands. The broader finding is that workspace quality, trajectory choice, actuator architecture, and closed-loop tracking are connected design decisions. Keeping alternative solutions until later stages can reveal differences that early selection would hide.

7 Limitations and Reproducibility

The proposed framework was evaluated using numerical simulations rather than experiments with a physical robot. The simulation model includes robot dynamics, gearbox effects, permanent-magnet synchronous motor (PMSM) electrical dynamics, field-oriented control (FOC), and computed-torque control (CTC). However, some effects that may influence the performance of a real robot are not included in the model.

First, the mechanical model assumes that the robot links and transmissions are rigid. It does not explicitly consider link flexibility, gearbox compliance, backlash, or other unmodeled mechanical effects. The friction parameters are also based on engineering assumptions rather than experimental measurements. Therefore, the tracking performance observed in simulation may differ from the performance of a physical robot.

Second, the electrical model does not fully represent inverter losses, magnetic losses, or motor heating. Field weakening is also not included. Consequently, the reported torque, current, speed, and voltage results are valid within the assumptions and limits of the adopted simulation model. A motor may briefly operate above its continuous rating without exceeding its permitted peak rating. However, meeting the short-duration operating limits does not guarantee that the motor can perform the same task repeatedly without overheating. Confirming repeated-duty operation would require a validated thermal model and additional testing.

The mechanical-work objectives used in trajectory optimization also differ from electrical-energy consumption. They measure the mechanical energy transferred at the robot joints but do not include all electrical losses or the effects of energy recovery during regenerative operation.

Third, the workspace analysis is based on a finite number of sampled joint configurations, together with targeted numerical refinement. The calculated convex-hull volume provides an outer boundary around the sampled workspace. It does not represent the exact usable workspace of the robot. Similarly, the reported measures of dexterity, payload sensitivity, and tool-center-point (TCP) position sensitivity describe the configurations examined in the study. They do not establish the performance of every possible robot configuration.

The Pareto results are also limited to the candidates, objectives, constraints, payload, and motion durations considered in the analysis. The screened workspace-Pareto subset is not a mathematically proven global Pareto frontier. Likewise, C3 and C24 are nondominated among the evaluated feasible

trajectories, not necessarily among all possible robot trajectories.

Fourth, the four-scenario Cartesian tracking comparison consists of two separate controlled comparisons. Scenarios A and B use the same H1 actuator architecture and G2 controller. Scenarios C and D use the same A218 actuator architecture and G2 controller. Therefore, the effects of changing the trajectory can be examined within each pair because the actuator architecture and controller remain unchanged. However, differences between the A/B and C/D groups cannot be explained by trajectory design alone, because the two groups use different actuator architectures.

Finally, the numerical results are supported by preserved simulation records, numerical datasets, and audited analysis files. These records allow the reported calculations and comparisons to be traced to the stored simulation evidence.

However, the exact binary versions of some historical simulation models could not be fully recovered or independently confirmed. Therefore, the study establishes traceability of the accepted numerical results and the documented methodology, but does not claim exact byte-for-byte reproduction of every historical simulation. These limitations define what can be concluded from the present study. They also identify the additional modeling, thermal analysis, and experimental validation needed before applying the framework to a physical robot.

8 Conclusion

This study developed an integrated simulation-based framework for analyzing the workspace, evaluating trajectories, selecting motor–gearbox architectures, and validating the electromechanical performance of a six-degree-of-freedom (6-DoF) manipulator carrying an 18-kg payload. The main contribution is a traceable task-to-actuator design process that considers competing engineering requirements across the different design stages.

The workspace analysis examined 50,000 sampled joint configurations. Two separate but overlapping groups were identified: 5,001 high-quality configurations and 1,094 screened workspace-Pareto configurations. These results show that a robot's ability to reach a position does not necessarily mean that it has good dexterity, low payload sensitivity, or favorable positioning capability at that position.

Trajectory generation was evaluated separately from workspace classification. Of the 24 generated candidate trajectories, 11 satisfied the joint-space continuity requirements, and eight also met the dense Cartesian position and orientation accuracy requirements. This shows that starting from a favorable robot configuration does not guarantee a feasible trajectory for the complete task.

The four-objective dynamic Pareto analysis retained two nondominated trajectories, C3 and C24. C3 required the lowest peak aggregate joint torque, while C24 had the lowest RMS aggregate torque, positive mechanical work, and absolute mechanical work. These results demonstrate the importance of comparing different performance objectives rather than selecting a trajectory using only one measure.

Both trajectories were considered during the manufacturer-constrained motor–gearbox search. Local dominance screening reduced approximately 1.178×10^{9} possible six-joint combinations to 1.347×10^{6} candidates before architecture-level Pareto evaluation. The A218 architecture was then selected as the common representative for detailed electromechanical simulation and validation.

The four-scenario letter-E experiment further showed how trajectory design affects closed-loop Cartesian tracking. Under the same H1 actuator architecture and G2 controller, replacing the sharp-corner trajectory with a rounded-corner trajectory reduced Cartesian root-mean-square error (RMSE) from 44.5767 to 3.4071 mm, representing an improvement of approximately 92.36%. Under the same A218 actuator architecture and G2 controller, the C24-associated trajectory reduced Cartesian RMSE from 1.9781 to 1.7411 mm compared with C3, an improvement of approximately 11.98%.

These results show that changing the trajectory can improve tracking performance even when the actuator architecture and controller settings remain unchanged. However, the differences between the H1 and A218 groups cannot be attributed to trajectory optimization alone, because the two groups use different actuator architectures.

Overall, the findings show that workspace quality, trajectory selection, actuator design, and closed-loop performance are closely connected. Considering these factors together, while preserving alternative design solutions, makes it possible to evaluate their combined effects before selecting a final robot design.

Future work will include experimental validation, more detailed models of transmission behavior and electrical losses, repeated-duty thermal analysis, and performance evaluation under parameter uncertainty and external disturbances. These studies will help establish how well the simulation results apply to physical robotic systems.

Declarations

Conflict of interest

The authors declare no competing interests.

Data availability

The reported numerical results are derived from preserved simulation records and audited result files. Further data are available from the corresponding author on request.

Funding

This work was supported by the Fundação de Amparo à Pesquisa do Estado de São Paulo (FAPESP), grant 2026/19488-3, under project grant 2020/15245-2. This study was financed in part by the Coordenação de Aperfeiçoamento de Pessoal de Nível Superior (CAPES), Brazil, Finance Code 001.

References

[1] Yoshiki Mori, Yudai Fukuzawa, Koji Matsuno, Ryosuke Nishida, Moyako Tachibana, Ryuhei Sakurai, Satoshi Okano, Zhongkui Wang, and Sadao Kawamura. Design methodology for workspace adjustment of industrial robot arms using a long end-effector: Implementation in a dish-washing robot system. *The International Journal of Advanced Manufacturing Technology*, 143:4249–4261, 2026. doi: 10.1007/s00170-026-17785-4. URL `https://doi.org/10.1007/s00170-026-17785-4`.

[2] Thais Campos Farley and Hadas Kress-Gazit. Automated task-based approach to modular manipulator design: Position accuracy and heavy payload capacity requirements. *Journal of Mechanisms and Robotics*, 2025. doi: 10.1115/1.4068240. URL `https://doi.org/10.1115/1.4068240`.

[3] Zehui Lu and Yebin Wang. A differentiable dynamic modeling approach to integrated motion planning and actuator physical design for mobile manipulators. *Journal of Field Robotics*, 42(1):37–64, 2025. doi: 10.1002/rob.22394. URL `https://doi.org/10.1002/rob.22394`.

[4] T. Bao, Z. Wu, and J. Chen. Multi-objective optimal trajectory planning for manipulators based on cmospbo. *Autonomous Intelligent Systems*, 4:22, 2024.

[5] S. Zhu, Y. Zhang, Z. Li, J. Wang, and S. Yuan. Multi-objective optimal trajectory planning method for robot manipulator with real-time parameters monitoring. *Mechanical Systems and Signal Processing*, 229:112518, 2025. doi: 10.1016/j.ymssp.2025.112518.

[6] Z. Xiao, D. Sun, D. Zhu, Y. Wang, Y. Yan, and H. Wu. Time–torque coordinated optimization for trajectory planning of industrial robots. *Robotics and Computer-Integrated Manufacturing*, 99:103199, 2026. doi: 10.1016/j.rcim.2025.103199.

[7] Jintao Ye, Lina Hao, and Hongtai Cheng. Multi-objective optimal trajectory planning for robot manipulator attention to end-effector path limitation. *Robotica*, 42(6):1761–1780, 2024. doi: 10.1017/S0263574724000481. URL `https://doi.org/10.1017/S0263574724000481`.

[8] J. L. Torres, M. Muñoz, J. D. Àlvarez, J. L. Blanco, and A. Gimenez. Robodimm: A web-based framework for trajectory-level dynamics and deterministic actuator sizing of industrial manipulators. *SoftwareX*, 35:102997, 2026. doi: 10.1016/j.softx.2026.102997.

[9] A. Stein, Y. Wang, Y. Sakamoto, B. Wang, and H. Fang. Application-oriented co-design of motors and motions for a 6dof robot manipulator. In *Proceedings of the IEEE Conference on Automation Science and Engineering (CASE)*, 2025. doi: 10.1109/CASE58245.2025.11164119.

[10] J.-T. Lin, Z. Lu, and Y. Wang. Closed-loop co-design of motors, motions, and feedback control for robotic manipulators. *Journal of Artificial Intelligence for Automation*, 1 (2):8, 2026. doi: 10.53941/jaia.2026.100008.

[11] Bruno Siciliano, Lorenzo Sciavicco, Luigi Villani, and Giuseppe Oriolo. *Robotics: Modelling, Planning and Control*. Advanced Textbooks in Control and Signal Processing. Springer, London, 1 edition, 2009. ISBN 978-1-84628-642-1. doi: 10.1007/978-1-84628-642-1. URL `https://doi.org/10.1007/978-1-84628-642-1`.

[12] Tsuneo Yoshikawa. Manipulability of robotic mechanisms. *The International Journal of Robotics Research*, 4(2):3–9, 1985. doi: 10.1177/027836498500400201.

[13] Zhiwei Zhao, Yan Jin, Paul Goodall, Andrew West, and Mark Price. Simultaneous dimension and tolerance design for robot manipulator considering cost and positioning accuracy reliability. *The International Journal of Advanced Manufacturing Technology*, 143:6509–6522, 2026. doi: 10.1007/s00170-026-17862-8. URL `https://doi.org/10.1007/s00170-026-17862-8`.

[14] Adam Wolniakowski, Charalampos Valsamos, Kanstantsin Miatliuk, Vassilis Moulianitis, and Nikos Aspragathos. Optimization of dynamic task location within a manipulator's workspace for the utilization of the minimum required joint torques. *Electronics*, 10(3):288, 2021. doi: 10.3390/electronics10030288. URL `https://doi.org/10.3390/electronics10030288`.

[15] Dithoto Modungwa. Enhanced concept-based exploration of manipulators' design spaces with kinematics, dynamics and control co-design. *Mathematical and Computational Applications*, 31(4):164, 2026.

[16] Kevin M. Lynch and Frank C. Park. *Trajectory Generation and Motion Planning*, pages 282–348. Cambridge University Press, 2017.

[17] Giuliano Fabris, Lorenzo Scalera, and Alessandro Gasparetto. The impact of kinematic redundancy on the energetic performance of robotic manipulators. *Robotics*, 15 (3):51, 2026.

[18] Kalyanmoy Deb. *Multi-Objective Optimization Using Evolutionary Algorithms*. John Wiley & Sons, 2001. ISBN 9780471873396.

[19] Kalyanmoy Deb, Amrit Pratap, Sameer Agarwal, and T. Meyarivan. A fast and elitist multiobjective genetic algorithm: NSGA-II. *IEEE Transactions on Evolutionary Computation*, 6(2):182–197, 2002. doi: 10.1109/4235.996017.

[20] The MathWorks, Inc. *MATLAB (Version R2026a)*. The MathWorks, Inc., Natick, Massachusetts, USA, 2026. URL `https://www.mathworks.com/products/matlab.html`.

[21] The MathWorks, Inc. *Simulink (Version R2026a)*. The MathWorks, Inc., Natick, Massachusetts, USA, 2026. URL `https://www.mathworks.com/products/simulink.html`.

[22] European Southern Observatory. MOSAIC – multi-object spectrograph for astrophysics, intergalactic-medium studies and cosmology. `https://elt.eso.org/instrument/MOSAIC/`, 2026. Accessed: 6 November 2026.

[23] Maxime Rombach, Markus Thurneysen, Lucas Ortolani, Jurgen Schmoll, Diane Chapuis, Malak Galal, Sebastien Pernecker, Cassio Berni, Ojonugwa Adukwu, Fabio Fialho, et al. Mosaic at elt: design and first performance results of novel robotic optical-relay positioners. *arXiv preprint arXiv:2606.20194*, 2026.

[24] Mark W. Spong, Seth Hutchinson, and M. Vidyasagar. *Robot Modeling and Control*. Wiley, 2 edition, 2020.

[25] Lauri Pyrhönen, Aki Mikkola, and Frank Naets. System identification and force estimation of robotic manipulator using semirecursive multibody formulation. *Multibody System Dynamics*, 64:167–194, 2025. doi: 10.1007/s11044-024-10017-1. URL `https://doi.org/10.1007/s11044-024-10017-1`.

[26] Analysis of different friction compensation methods in the context of a flexible joint robot, 2025. URL `https://research.tue.nl/files/312301713/1608770_-_Friction_Compensation_Methods.pdf`. Eindhoven University of Technology, Section 2, Equation (2.4) .

[27] Yutong Wang, Junjie Li, Ke Wang, and Shaokun Wang. Design and analysis of modular reconfigurable manipulator system. *Mathematics*, 13(7):1103, 2025.

[28] Yao Sun, Yi Wan, Haifeng Ma, and Xichang Liang. Workspace description and evaluation of master-slave dual hydraulic manipulators. *Actuators*, 12:9, 2022.

[29] Ramkumar Natarajan, Garrison LH Johnston, Nabil Simaan, Maxim Likhachev, and Howie Choset. Torque-limited manipulation planning through contact by interleaving graph search and trajectory optimization. In *2023 IEEE International Conference on Robotics and Automation (ICRA)*, pages 8148–8154. IEEE, 2023.

[30] Yaohua Zhou, Chin-Yin Chen, Ye Tang, Hongyu Wan, Jingbo Luo, Guilin Yang, and Chi Zhang. A comprehensive on-load calibration method for industrial robots based on a unified kinetostatic error model and gaussian process regression. *IEEE Transactions on Instrumentation and Measurement*, 73:1–11, 2024.

[31] Zhiwei Zhao, Yan Jin, Paul Goodall, Andrew West, and

Mark Price. Simultaneous dimension and tolerance design for robot manipulator considering cost and positioning accuracy reliability. *The International Journal of Advanced Manufacturing Technology*, 143(11):6509–6522, 2026.

[32] Arturo Franco-López, Mauro Maya, Alejandro González, Liliana Félix-Ávila, César-Fernando Méndez-Barrios, and Antonio Cardenas. Robust optimization and workspace enhancement of a reconfigurable delta robot via a singularity-sensitive index. *Robotics*, 15(1):11, 2025.

[33] Eckart Zitzler, Kalyanmoy Deb, and Lothar Thiele. Comparison of multiobjective evolutionary algorithms: Empirical results. *Evolutionary Computation*, 8(2):173–195, 2000. doi: 10.1162/106365600568202.

[34] Kaisa Miettinen. *Nonlinear Multiobjective Optimization*. International Series in Operations Research & Management Science. Kluwer Academic Publishers, 1998. ISBN 9780792382782. doi: 10.1007/978-1-4615-5563-6.

[35] Matthias Ehrgott. *Multicriteria Optimization*. Springer, Berlin, Heidelberg, 2 edition, 2005. ISBN 9783540213987. doi: 10.1007/3-540-27659-9.

[36] P. Pillay and R. Krishnan. Modeling, simulation, and analysis of permanent-magnet motor drives. part i: The permanent-magnet synchronous motor drive. *IEEE Transactions on Industry Applications*, 25(2):265–273, 1989. doi: 10.1109/28.25541.

[37] Bimal K. Bose. *Modern Power Electronics and AC Drives*. Prentice Hall PTR, Upper Saddle River, NJ, USA, 2002. ISBN 9780130167439.

[38] Mark W. Spong, Seth Hutchinson, and M. Vidyasagar. *Robot Modeling and Control*. John Wiley & Sons, Hoboken, NJ, USA, 2006. ISBN 9780471649908.

[39] Karl J. Astrom and Bjorn Wittenmark. *Computer-Controlled Systems: Theory and Design*. Prentice Hall, 3 edition, 1997. ISBN 0133148998.